Stability and energetics of two-dimensional surface crystals in liquid AuSi thin films and nanoscale droplets

Hailong Wang,[1,*] Mengyuan Wang,[1] Alireza Shahabi,[2] Alain Karma,[3] and Moneesh Upmanyu[2,†]

[1]*CAS Key Laboratory of Mechanical Behavior and Design of Materials, Department of Modern Mechanics, CAS Center for Excellence in Complex System Mechanics, University of Science and Technology of China, Hefei, Anhui 230027, China*

[2]*Group for Simulation and Theory of Atomic-Scale Material Phenomena (stAMP), Department of Mechanical and Industrial Engineering, Northeastern University, Boston, Massachusetts 02115, USA*

[3]*Department of Physics, Northeastern University, Boston, Massachusetts 02115, USA*

(Received 28 February 2020; accepted 12 May 2021; published 12 July 2021)

We employ atomic-scale computational frameworks to study the surface crystallization in AuSi films and droplets as a function of composition, temperature, and size. Above the melting point, the surfaces of both thin films and droplets undergo a first-order transition from a two-dimensional (2D) Au_2Si crystalline phase to a laterally disordered yet stratified layer. The thin film surfaces exhibit an effective surface tension that increases with temperature and decreases with Si concentration, while for droplets in the size range 10–30 nm, the bulk Laplace pressure alters the surface segregation as it occurs with respect to a strained bulk. Above the transition, the size effect on the surface tension due to the stratified surface layer is small, while the crystalline surface layer below the transition is strained and composed of 2D crystallites separated by extended grain boundary scars that lead to large fluctuations in its energetics. As a specific application, all-atom simulations of AuSi droplets on Si(111) substrate subject to Si surface flux show that the supersaturation dependent surface tension destabilizes the contact line *via* formation of a precursor wetting film on the solid-vapor interface and has ramifications for size selection during droplet-catalyzed routes for nanowire growth. Our study sheds light on the interplay between stability and energetics of surfaces in this unique class of binary alloys and offers pathways for exploiting their surface structure for varied applications such as catalytic nanocrystal growth, dealloying, and polymer crystallization.

DOI: 10.1103/PhysRevMaterials.5.074003

I. INTRODUCTION

Metal-covalent alloys form a versatile class of multifunctional material systems as their properties vary fundamentally with composition, from metallic alloys and amorphous glasses to crystalline semiconductors. These alloy systems often form low-melting eutectics that serve as nanoscale catalysts for the growth of low-dimensional crystalline nanostructures such as semiconducting nanowires, inorganic nanotubes, and nanoribbons. Examples of such nanostructure-catalyst systems include Si/Ge-Au, Si-Al, GaN/GaAs/GaP-Au/Ni, ZnO-Au, C/Co, C/Fe [1–3]. Several of these systems also serve as precursors for dealloying based routes for synthesis of nanoporous films and particles for catalysis and energy storage [4–6]. The synthesis of these nanocrystals requires catalytic breakdown of the precursor gases on their surfaces at temperatures that usually exceed their melting points. The chemistry, structure, and morphology of the liquid surfaces has a decisive effect on crystal nucleation and growth and therefore directly impacts the quality of the as-grown nanostructures.

Past thin film studies have shown that the surfaces of several binary liquids are nonclassical [7–9]. The surface is stratified, and in specific systems such as AuSi employed for the growth of Si nanowires (SiNWs), segregation triggers the crystallization of a solidlike surface layer that is stable above the bulk melting point. Experimental studies on thin films have shown that the surface is Si-rich relative to the bulk [10,11]. At near-eutectic temperatures, it is ordered preferentially through the thickness and capped with a laterally ordered crystalline layer [7,8]. A similar ordered surface structure was observed in computations on nanoscale AuSi droplets [12] and in experiments [13], suggesting that this phenomenon of surface crystallization is resilient to large surface curvatures. These examples of stratification and crystallization on liquid surfaces are atomically thin limits of interfacial layering and premelting/prefreezing reported in metallic and molecular liquids, amorphous solids, and linear chain polymers [14–19], wherein the interfacial structural transitions often result in low-dimensional phases unlike their bulk counterparts.

The surface structure and chemistry has obvious implications for catalysis as they both affect the chemical breakdown of the precursor gases on thin films and droplets. They also modify the surface energetics and this is an equally important aspect for the stability of supported droplets; the effective surface tension γ_{lv} is a key ingredient for the Young's balance

*hailwang@ustc.edu.cn
†mupmanyu@northeastern.edu

at the enveloping contact line formed by the intersection of two additional interfaces: substrate/crystal solid-vapor interface γ_{sv} and substrate/crystal-particle solid-liquid interface γ_{sl}. During vapor-liquid-solid (VLS) growth of SiNWs for example, the resultant droplet morphology sets the surface chemical potential of the growing species. It controls the dynamics of the supersaturation that develops within the droplets and therefore impacts the size and orientation selection of the nanocrystals [20–22], aspects that are crucial for the controlled and scalable synthesis of these nanostructures *via* liquid mediated routes.

In this study, we employ atomic-scale computational approaches to explore the interplay between surface structure and surface tension γ_{lv} of the surfaces of AuSi thin films and nanoscale droplets. The material system is motivated by the fact that AuSi nanoparticles continue to be important for scalable growth of SiNWs due to the combination of a low-melting eutectic point [$X^E_{Si} = 19\%, T_E = 636$ K] and negligible solubility below the eutectic temperature. More generally, it is a representative material system for fundamental studies on the VLS route for growth of semiconducting nanowires and related nanostructures, for crystal nucleation and growth at the nanoscale [23–30], surface catalysis, and for understanding the stability and dynamics during templated alloying and dealloying [6].

The article is organized as follows: We first quantify the liquid surface energetics at and near-equilibrium by analyzing the surface structure and extracting the surface tension as a function of the growth temperature and droplet composition, $\gamma_{lv} \equiv \gamma_{lv}(X_{Si}, T)$. The computations are performed for both thin films and droplets with varying radii to capture the size effect, $\gamma_{lv} \equiv \gamma_{lv}(R)$. As self-consistent validation of the results, we perform simulations of AuSi droplets on Si substrates and compare their stability at equilibrium, and under near-equilibrium conditions by subjecting the droplet surfaces to a steady-state Si flux. We conclude with a discussion of the results as they relate to VLS growth of semiconducting nanowires, and more general catalytic growth of crystalline nanofilaments.

II. COMPUTATIONAL METHODS

The atomic-scale computations are based on a recently developed AuSi empirical interatomic potential [12,31]. The classical approximation is crucial as it allows access to length- and time-scales necessary for extraction of surface structures and surface tension. The potential accurately predicts the stability of AuSi clusters and droplets and is tailored to reproduce the binary Au-Si phase diagram [12]. In particular, it recovers the signature low-melting eutectic, with a eutectic point ($T_E = 590$ K, $X^E_{Si} = 33\%$) that is in good agreement with experiments.

The classical approach employed to extract the structure and energetics of liquid surfaces is based on equilibrium molecular dynamics (MD) simulations of near-eutectic AuSi alloys. The simulations are performed for thin film and nanoscale droplet geometries and for temperatures and compositions in the range $T = 590{-}1100$ K and $X_{Si} = 20{-}45\%$, respectively. For both classes of simulation geometries, the initial configuration consists of a randomly mixed alloy with prescribed composition X_{Si} and mean interatomic distances corresponding to the liquid alloy density. Semi-grand canonical Monte Carlo (SGMC) simulations followed by MD simulations are employed to obtain a fully equilibrated alloy [32]. The SGMC equilibration is modified to preserve the stoichiometry via a combination of translational and exchange moves (ratio fixed at 1:10). Typically, this extends to tens of million translation steps. To further equilibrate the structure at the desired temperature, the SGMC output is subject to additional canonical MD simulations in excess of a nanosecond using a Nöse-Hoover thermostat [33] with a fixed time step of 1 fs. This sequence of simulations is performed until the interaction energy and surface density profiles converge.

Alternatively, in all of the cases, we have performed the equilibration directly with MD, and the results reliably converge to those obtained by SGMC simulations in less than a nanosecond. Data runs performed following equilibration consist of equilibrium MD simulations for an average of 10 ns, and the configurations are stored every 10 time steps for structural analyses.

A. Through thickness density profiles

The density profiles in this films are extracted within slices each of thickness $\delta z = 0.05$ Å along the surface normals. The range of these slices is large enough to include all the atoms during the computations. The number of atoms in each slice $n(z, t)$ is recorded every 10 time steps, where z is the depth coordinate of each slice and t is the simulation time. The density within each slice is reported as a time average over multiple equilibrium configurations,

$$\rho(z) = \frac{1}{\tau}\sum_{i=1}^{\tau}\frac{n(z, t_i)}{V(z)}, \tag{1}$$

where $V(z)$ is the volume of each slice. The density profiles are extracted with respect to the surface whose location $h(x, y, t) \equiv h(x, y)$ is defined as

$$\int_{z_0}^{\infty}[\rho(z) - \rho_b(z)]dz = 0,$$

with $\rho_b = \rho_l$ for $z < h(x, y)$ and $\rho_b = \rho_v$ for $z > h(x, y)$. Here ρ_l and ρ_v are the densities of the bulk liquid and the vapor, respectively. This study is limited to droplet-vacuum surfaces, i.e., $\rho_v = 0$. The reference depth z_0 is spatially averaged over each of the N_s slices,

$$z_0 = \frac{1}{N_s}\sum_{i=1}^{N_s} z_i.$$

For droplets, the atoms are partitioned into radial shells with thickness $\delta r = 0.05$ Å, where the coordinate r of each shell is defined with respect to the spatially averaged center of mass of the droplet. As in thin films, the range of these shells is large enough to include all the atoms at any time during the simulations, and the number of atoms in each shell $n(r, t)$ is extracted every 10 time steps. The density of each shell is extracted based on Eq. (1), with the surface of the droplet defined as

$$\int_{0}^{\infty}[\rho(r) - \rho_b(r)]r^2dr = 0, \tag{2}$$

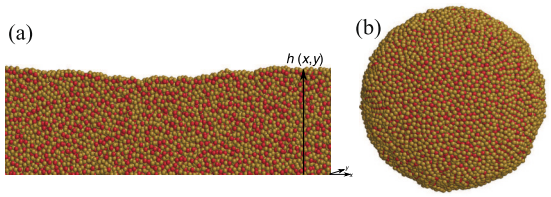

FIG. 1. Atomic configurations of (a) AuSi thin slabs and (b) AuSi droplets used in this study, equilibrated at $X_{Si} = 0.33\%$ and $T = 873$ K. (a) Cross section of a ribbonlike liquid slab showing morphological fluctuations of one of the two surfaces. Cubic liquid slabs are used for extracting the surface stresses (not shown). (b) Liquid droplets used for extracting size-dependent surface tension. Here and elsewhere, red and gold colors denote Si and Au atoms, respectively.

with $\rho_b = \rho_l$ for $r < R_e$ and $\rho_b = \rho_v$ for $r > R_e$.

The surface segregation in thin films and droplets is quantified by extracting the through-thickness variation of the normalized density $\rho(z)/\rho_0$. Here ρ_0 is the average density defined as

$$\rho_0 = \frac{N}{V},$$

with N the number of atoms, and V is volume. The latter is taken to be the volume of the equilibrated computational cell for thin films, while for droplets it is based on the droplet radius, $V = 4\pi R_e^3/3$.

B. Capillary fluctuation method

The surface tension of the thin films is extracted from the power spectrum of the surface capillary waves, based on the capillary fluctuation method (CFM) [34,35]. The fluctuations in profiles of a free liquid-vapor (vacuum) surface is monitored and time-averaged over uncorrelated atomic configurations. In the limit of small slopes, decomposition in Fourier space yields a mode dependent fluctuation amplitude,

$$\langle |A(k)|^2 \rangle = \frac{k_B T}{A_s k^2} \frac{1}{\gamma + \gamma''}, \tag{3}$$

where $A_s = bl$ is the projected surface area and $\gamma + \gamma''$ is the surface stiffness. For liquid surfaces with inclination independent energetics, the stiffness is the surface tension of the planar film, $\gamma + \gamma'' = \gamma_{lv}^0$.

Simulations of liquid slabs with ribbon-like geometries each of length $l = 50$ nm and thickness $b \approx 2$ nm are used to extract the fluctuation spectrum. Periodic boundary conditions are applied in-plane (x-y) and the two z surfaces are held free. In total, the size of each simulation is ≈80 000 atoms. Varying the film thicknesses above $h \approx 25$ nm ensures that the two free surfaces do not interact, and the surface structure is size independent. As an example, Fig. 1(a) shows one of the two fluctuating surfaces with $X_{Si} = 33\%$ at $T = 873$ K. For each slab, the surface profile $h(x, y)$ is extracted by monitoring the positions of the surface atoms and the surface structure is characterized by the local density within slices of thickness 0.05 Å.

C. Surface stress method

An alternate approach is based on the relation between the surface tension and the stress state of liquid surfaces [36,37]. The mechanical definition takes the form

$$\gamma_{lv}^0 = \frac{1}{2}(\sigma_{xx}^s + \sigma_{yy}^s - 2\sigma_{zz}^s), \tag{4}$$

where $\sigma_{\alpha\beta}$ is surface stress tensor, $(\alpha, \beta) \equiv (x, y, z)$. Its components are calculated from the atomic interactions and the trajectories of the surface atoms based on the atomistic virial stress tensor [38]. Unlike the ribbon-like slab geometry used for CFM simulations, fluctuations in surface morphology are undesirable as they lead to spatial variations in the surface stresses. The fluctuations decay with the surface aspect ratio [39] and we therefore employ 8.5 nm × 8.5 nm × 8.5 nm cubic slabs for this class of simulations. Size effect studies with larger simulation sizes yield converging surface structures and surface tension. The surface stresses are monitored in surface slices of thickness 0.05 Å within equilibrium MD simulations.

D. Laplace pressure method

The size dependence $\gamma_{lv}(R)$ is studied by performing similar computations on isolated nanoscopic droplets. Figure 1(b) shows the atomic configuration of one such droplet with bulk composition $X_{Si} = 33\%$ at $T = 873$ K. For a droplet in equilibrium with its vapor, the (bulk) Laplace pressure that balances the surface capillary forces is related to the surface tension by the well-known Gibbs-Thomson equation [40,41],

$$\Delta P = \frac{2\gamma_{lv}^0}{R_e}\left(1 - \frac{\delta}{R_e} + \dots\right), \tag{5}$$

where γ_{lv}^0 is the surface tension of a planar surface and R_e is the equimolar droplet radius based on the definition Eq. (2). The surface tension can then be expressed as

$$\gamma_{lv} = \gamma_{lv}^0\left(1 - \frac{2\delta}{R_e} + \dots\right), \tag{6}$$

and the extent of the size dependence is captured by the length scale δ, also known as the Tolman length [42]. The pressure differential across the droplet surface is calculated using the virial stress within the bulk,

$$\Delta P = -\frac{1}{3}(\sigma_{xx} + \sigma_{yy} + \sigma_{zz}), \tag{7}$$

where the stresses $\sigma_{\alpha\beta}$ are components of the atomistic virial stress tensor [38]. The density and Laplace pressure are recorded in shells with thickness 0.1 nm every 10 time steps. The simulations are performed for droplets with varying sizes in the range $2R = 10$–30 nm (32,000–256,000 atoms). Comparisons with the thin film computations are made to quantify the size effect.

III. RESULTS

A. Thin films

Surface segregation is evident in the sectional view of the liquid slab shown in Fig. 1(a). We quantify it by extracting the through-thickness variation of the normalized density $\rho(z)/\rho_0$ of both Au and Si. Figure 2(a) shows the variation averaged

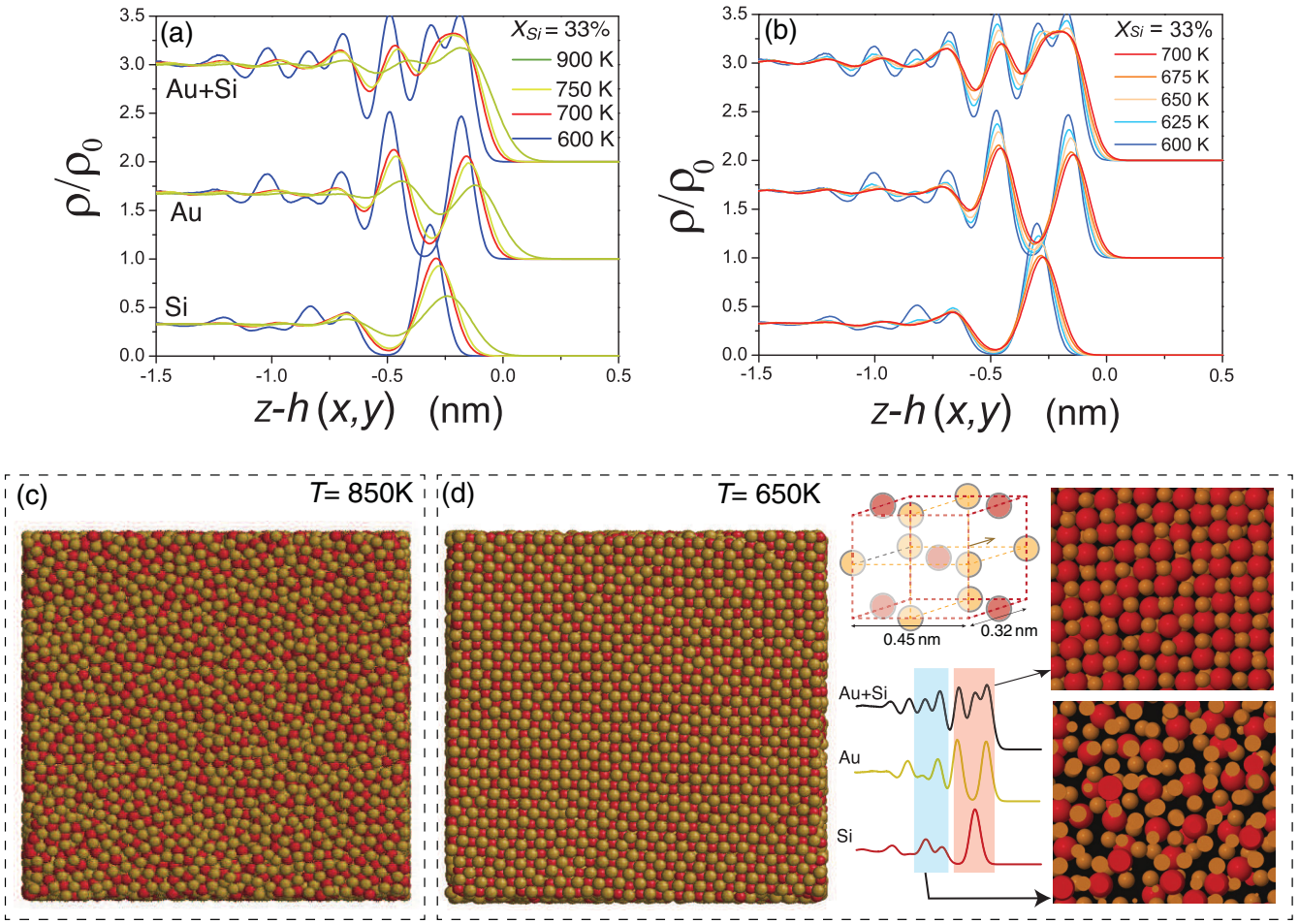

FIG. 2. (a) Through thickness variations of density profiles $\rho_{\mathrm{Au+Si}}(z)$, $\rho_{\mathrm{Au}}(z)$, and $\rho_{\mathrm{Si}}(z)$ in liquid AuSi slabs extracted using equilibrium MD simulations, for varying temperatures at $X_{\mathrm{Si}} = 33\%$. The profiles are calculated with respect to the local height profile $h(x, y)$ of the film and averaged over the two free surfaces. The component plots are shifted along the vertical axis for clarity. The densities are normalized to the atom number densities of bulk alloys at the corresponding composition and temperature. (b) Same as in Fig. 2(a) but for a narrower temperature range, $T = 600-700$ K. [(c)–(d)] Characterization of the surface structure observed in thin film computations at (c) 850 K and (d) 650 K. [(d), top right] The Au_2Si unit cell associated with the lateral ordering of the surface layer. The arrow indicates the orientation of the surface normal. [(d), bottom right] The overall and component density profiles within 0.32-nm-thick surface and subsurface layers shaded light red and blue, respectively. The atomic configurations of the two layers are also shown in the right panel. See text for details.

over the two thin films surfaces at the eutectic composition $X_{\mathrm{Si}} = 0.33\%$ and at varying temperatures above the bulk melting (eutectic) point, $T_m(= T_E)$. In all instances, the surface is on average denser compared to the bulk, consistent with recent *ab initio* and classical MD simulations [11,12]. Closer examination of the density profiles near the surface reveals peaks in Au and Si densities.

At higher temperatures $T > 800$ K, the component density profiles indicate subsurface Si segregation relative to the bulk that alternates with smaller Au peaks, characteristic of a stratified surface layer. Examination of the surface structure reveals that lateral order along the film surface is absent, evident in the top view of the surface at $T = 850$ K [Fig. 2(c)]. The surface is capped by a Au submonolayer, consistent with the sustained catalysis of Si precursors on these surfaces as well as the stability of Au adatoms on Si-rich surfaces [43]. Lowering the temperature has a dramatic effect on the density profiles. The Si and Au surface peaks increase in their intensity. Consequently, the surface excess and the through-thickness order are both enhanced. The extent over which the peaks decay into the bulk also increases, signifying an increase in the overall depth of the surface stratification. Below $T \approx 750$ K, we observe lateral crystallization along the surface and the capping Au layer transitions to an ordered monolayer. The long-range order extends to the Si-rich subsurface based on the surface peaks in the overall density profiles, also visible in the top view of one of the free surfaces at $T = 650$ K [Fig. 2(d)]. The density profiles reveal that the crystallization enhances through-thickness density of the surface layer. For example, we see the emergence of a bilayer peak in the density profile composed of the Si layer and the capping Au layer. The thickness of the crystallized layer is 0.32 ± 0.02 nm and does not vary with temperature. Careful examination of surface slices reveals a 2D square Si lattice (point group $p4m$) with a lattice parameter $a = 0.32$ nm, sandwiched by two identically structured Au-lattices shifted by one-half the lattice parameter. Taken *in toto*, the three layers order into an A(Au)-B(Si)-A(Au) stacking sequence [top right, Fig. 2(d)];

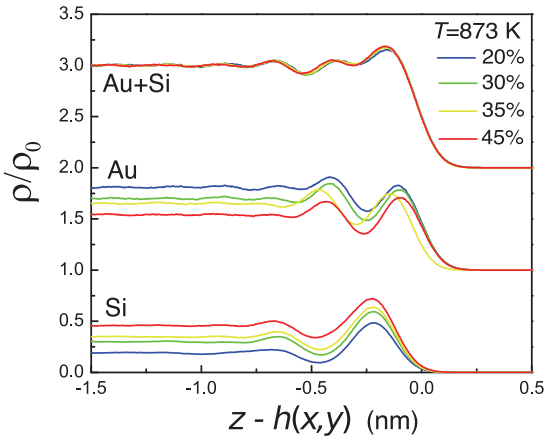

FIG. 3. Same as in Fig. 2(a) but for varying compositions at $T = 873$ K.

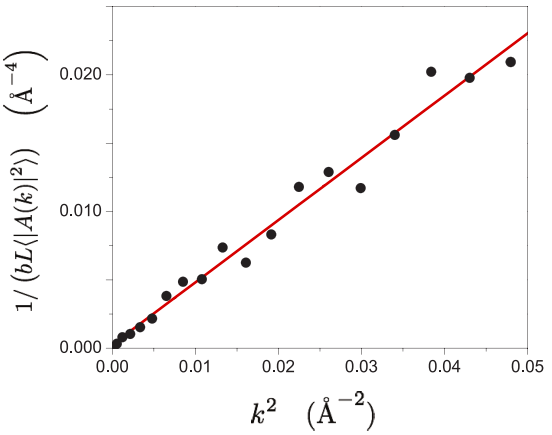

FIG. 4. Ensemble averaged fluctuation spectrum $1/\langle|A(k)|^2\rangle bW$ vs. k^2 of the two surfaces for the liquid slab shown in Fig. 1, for $X_{Si} = 33\%$ and at $T = 873$ K. The slope of the linear fit yields the surface tension, $\gamma_{lv}^0 = 0.58 \pm 0.02$ J/m^2.

a schematic of the Au_2Si unit cell and its surface orientation is also shown in the figure. The surface structure is unlike any bulk crystalline phase in this system. It is close to the Au_3Si_2 structure reported in *ab initio* simulations of $Au_{70}Si_{30}$ liquid [11] but differs from past reports on the structure of low and high temperature AuSi surface phases extracted using grazing incidence x-ray diffraction [8,44], primarily due to the presence of the capping Au monolayer. Immediately below the crystalline layer, the surface is stratified yet laterally disordered [right, Fig. 2(d)], and the disorder increases away from the surface. The trend is consistent with density profiles shown in Fig. 2(a).

Unlike the crystallized layer, the thickness of the stratified layer below markedly increases as the temperature approaches the bulk melting point. To see this clearly, Fig. 2(b) shows the density profiles for a narrower range of temperatures, from $T = 600-700$ K. The component profiles show emergence of new peaks away from the surface within the liquid, indicative of stratification into Au- and Si-rich layers as the temperature decreases. We see a sharp increase in the extent of stratification below 650 K. The crystallized layer does not exhibit significant changes in its density, consistent with the stability of this low temperature surface phase [8,13,44].

Increasing X_{Si} has a qualitatively different effect. Figure 3 shows the density profiles with varying composition at $T = 873$ K. The surface is stratified but laterally disordered indicating that the temperature is above the surface crystallization temperature for these compositions. The overall density profile as well as the width of the ordered surface layer do not change significantly, yet the surface becomes increasingly Si rich. As the temperature is lowered below $T \approx 750$ K, we again see the appearance of laterally ordered surface layer. The thickness of the 2D crystal does not change significantly within the range of compositions explored here, indicating that the changes in the Si excess at the surface are confined to the subsurface stratified layers.

We delegate a detailed structural characterization of the surface crystal to a later study, and extract the effective surface tension as a function of temperature and composition by monitoring the fluctuations and surface stresses in the liquid slabs. Figure 4 shows the fluctuation spectrum at $X_{Si} = 33\%$ and $T = 873$ K. The surface fluctuations are statistically significant, in particular the long wavelength (small k) amplitudes extend to several interatomic distances over the nanosecond-scale simulations. The spectrum is representative of the behavior observed for all composition ranges at $T = 873$ K in that $(\langle|A(k)|^2\rangle A_s)^{-1}$ increases linearly with k^2, i.e., the mean square amplitude $\langle|A(k)|^2\rangle$ decays as k^{-2} and the stratified surface behaves as a classical liquid surface [35]. Following Eq. (3), the slope yields the thin film surface tension, $\gamma_{lv}^0 = 0.58 \pm 0.02$ J/m^2.

The variation in planar-film surface tension with composition extracted using CFM is plotted in Fig. 5(b). Increasing X_{Si} lowers the surface tension and the sensitivity is higher for hypoeutectic alloys: $\gamma_{lv}^0 = 0.64$ J/m^2 for $X_{Si} = 20\%$ and it decreases to $\gamma_{lv}^0 = 0.58$ J/m^2 for $X_{Si} = 33\%$. Above the eu-

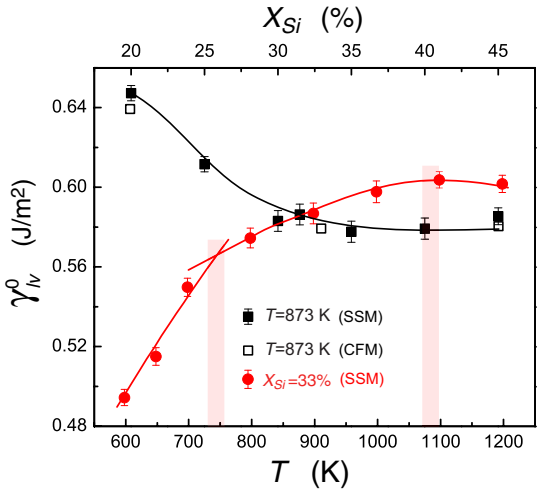

FIG. 5. Temperature and composition dependence of the planar AuSi surface tension γ_{lv}. The composition dependence is extracted at $T = 873$ K using CFM (open black squares) and SSM (solid black squares). The temperature dependence is extracted at $X_{Si} = 33\%$ using SSM (solid red circles). The two shaded temperature intervals represent distinct changes in the temperature dependence, $d\gamma_{lv}/dT$.

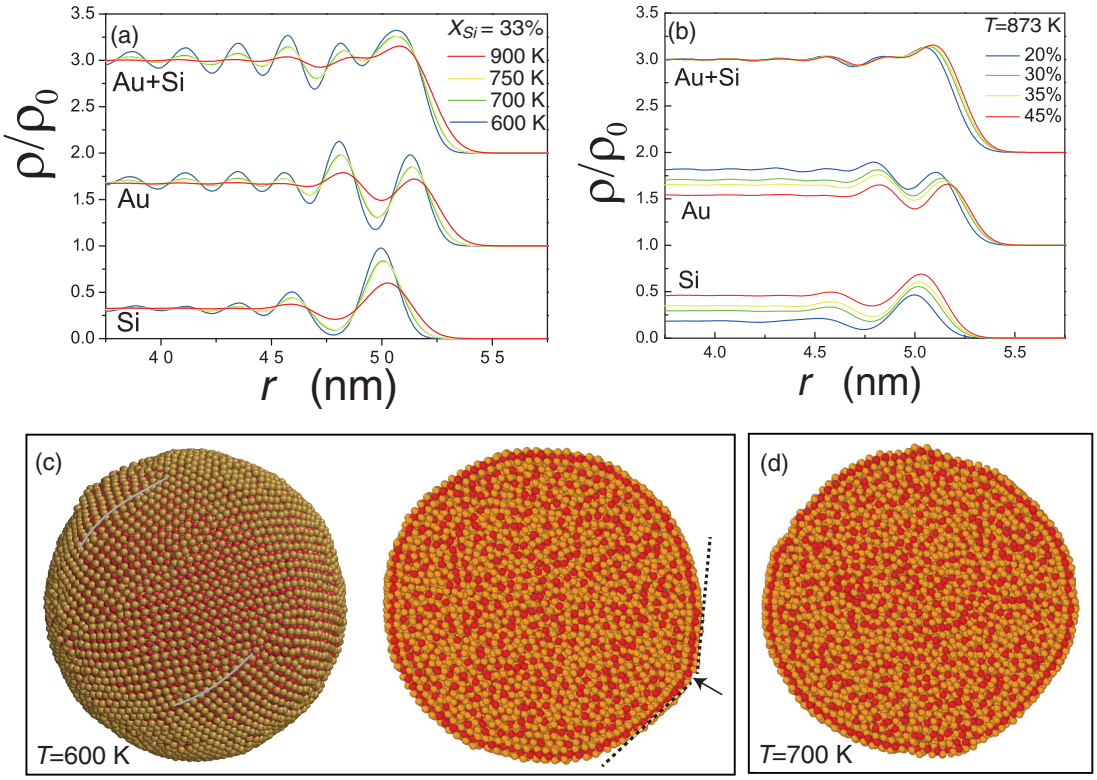

FIG. 6. Radial variation of the normalized density profiles $\rho(r)/\rho_0$ for a $2R = 10$ nm AuSi droplet, for the same set of temperatures and compositions as in Fig. 2(a) and Fig. 3. [(c), left] Atomic configuration of a $2R = 10$ nm droplet equilibrated at $T = 600$ K. The Au surface monolayer consists of ordered domains separated by finite length grain boundaries or grain boundary scars [45]. Two such instances of these surface defects are indicated (solid gray lines). Note the segregation of surface Au atoms at these extended defects. [(c), right] Midsection of the droplet that shows the surface segregation and crystallization. (d) The midsection of the droplet shown in (d) but at $T = 700$ K.

tectic composition, the decrease is smaller and for $X_{\rm Si} \geqslant 42\%$, the trend is reversed as the surface tension exhibits a small increase with concentration. The minimum in the surface tension corresponds to $\gamma_{\rm lv}^0 \approx 0.58$ J/m^2 over the composition range $X_{\rm Si} = 33{-}40\%$.

The surface fluctuations of the surface become increasingly suppressed at lower temperatures. We therefore rely on the surface stress method (SSM) to extract the temperature dependence $\gamma_{\rm lv}(T)$. As validation, the compositional variation extracted *via* SSM is in excellent agreement with the CFM results over the entire composition range (Fig. 5). The temperature dependence at fixed composition $X_{\rm Si} = 33\%$ is also plotted in Fig. 5. At $T = 600$ K, just above the eutectic temperature ($T/T_m = 1.02$), the surface tension is quite low, $\gamma_{\rm lv}^0 = 0.49$ J/m^2. It *increases* with temperature and then saturates to a value of $\gamma_{\rm lv}^0 = 0.61$ J/m^2 above ≈ 1050 K. The increase in the surface tension with temperature (slope $d\gamma_{\rm lv}/dT > 0$) is a signature of surface prefreezing. Our results show that while the width of crystallized surface layer does not diverge as we approach $T = T_m$, the thickness of the stratified layer of the adjoining liquid layers increases, analogous to the thermodynamic behavior of a prefrozen surface layer.

The surface tension does not increase uniformly with temperature. Rather we observe two regimes with characteristic values of $d\gamma_{\rm lv}/dT$ separated at $T \approx 750$ K. Since the slope is an indirect measure of the order within the layer, the transition signifies a change in the extent of crystalline order within the surface layer, quite possibly a slow order-disorder transition from a fully crystallized surface layer to a laterally disordered yet stratified surface.

B. Nanoscale droplets

We now turn our attention to the surfaces of nanoscale AuSi droplets. The large surface curvatures in these droplets can lead to changes in the structure of surface crystallized and stratified layers. Additionally, unlike thin films, the Laplace pressure within the droplet induced by the surface tension changes the melting temperature (Gibbs-Thomson effect) and can modify the relative molar volumes of Au and Si at the surface and within the bulk, leading to changes in the surface segregation and the surface tension.

We first study the composition and temperature dependence of the surface structure. Figures 6(a) and 6(b) show the temperature and composition dependence of the radial density profile $\rho(r)/\rho_0$ within a $2R = 10$ nm diameter AuSi droplet. The surface consists of terminating Au submonolayer with alternating Si-rich and Au-rich subsurface layers, similar to the surface structure observed for thin films. At $T = 873$ K, the subsurface is again silicon rich and gradually decays to the bulk composition. The intensities of the Si and Au peaks and the thickness of the ordered surface layer both increase with decreasing temperature.

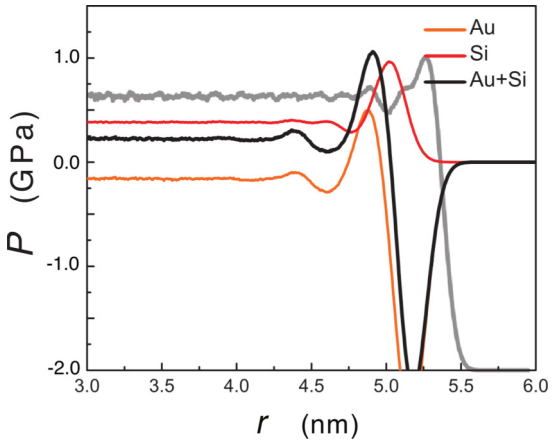

FIG. 7. Radial distribution of the virial pressure $P_{Au+Si}(r)$, $P_{Au}(r)$, and $P_{Si}(r)$ within a $2R = 10$ nm diameter AuSi droplet at $X_{Si} = 33\%$ and 873 K. The gray solid line is the corresponding overall density profile (scale not shown) that is superposed to help correlate the pressure distribution to the surface crystallization.

As the droplet is cooled closer to the eutectic temperature, we see the appearance of long-range lateral order at the surface, visible in the equilibrium droplet configuration at $T = 600$ K shown in Fig. 6(c). The corresponding midsection configuration reveals that the crystallization is limited to the surface with stratification in the underlying liquid. The surface crystal consists of perfect domains of crystallized layers separated by extended defects. These domains prefer to be planar and give an appearance of being faceted. This is likely due to the large surface curvature of the droplet that is geometrically accommodated by point and extended defects within the crystallized surface layer. Specifically, we see the appearance of several surface grains separated by finite length quasi-2D grain boundaries [Fig. 6(c)], not unlike the geometrically necessary grain boundary scars observed within crystals on spherical surfaces [45]. Two such intersecting domains separated by the core of a grain boundary scar are indicated in the midsection in Fig. 6(c). On increasing the temperature, these domains become less planar, consistent with decreasing crystalline order within the surface layer and decreasing surface density of the scars. As a direct comparison, Fig. 6(d) also shows the same midsection within a droplet equilibrated at $T = 700$ K.

While the overall trends in the behavior are qualitatively similar to that observed in thin films, there are some important deviations. Comparisons with density profiles for thin films at comparable temperatures [Fig. 6(a) and Fig. 2(a)] show that the peak intensities associated with surface segregation are smaller for the droplets. Near T_E, the ordering within the surface layers is relatively suppressed. Furthermore, although the compositional variation is qualitatively unchanged in that the subsurface becomes Si-rich with increasing X_{Si} [Fig. 6(b)], unlike thin films the Au and Si peaks at the surface shift outward as their intensity changes, consistent with expansion of the ordered surface layer, possibly driven by changes in the surface stress state relative to the thin films.

To develop an understanding of these variations, we characterize the stress distribution within the droplets. Figure 7 shows the radial distribution of the virial pressure within a droplet with $X_{Si} = 33\%$ and at $T = 873$ K. To help correlate the pressure distribution with the segregation profile, the overall normalized density distribution is also shown in the plot. The Laplace pressure is constant and positive for $r < 4.2$ nm. The pressure at the surface varies nonmonotonically within a 1.2-nm-thick layer. The ensemble averaged pressure difference across the entire surface layer is $\langle \Delta P \rangle \approx 0.2$ GPa. Examination of the component variations show that the Si-rich subsurface is compressive ($P > 0$) while the capping Au monolayer results in tensile stresses ($P < 0$). The nonmonotonic variations in the pressure are strongly correlated with segregation at the surface. Examination of the component density profiles (not shown) confirms that in general Si excess is associated with compressive stresses while Au excess counteracts their build up. Accordingly, the subsurface stratification of Si is associated with compressive stresses while the capping Au monolayer is under tension.

The density profiles and pressure distributions are similar for droplets in the size range studied here, $2R = 10-30$ nm. The range is large enough such that the surface segregation does not modify the composition in the bulk [46]. Figure 8(a) shows the radial variation of the density profiles at $X_{Si} = 33\%$ and at $T = 873$ K. The profile in the planar thin films is also plotted for comparison. The segregation profile for the largest droplet simulated here ($2R = 21.2$ nm) deviates significantly from that for the planar thin film, suggesting that the effect of the surface curvature is significant. The reduced intensities of the surface peaks indicate that the large surface curvature suppresses both Si and Au segregation to the surface, thereby reducing the through thickness stratification of the droplet surface. Decreasing the droplet size results in an increase in the intensity of the surface and subsurface peaks as well as an increase in the equimolar radii, implying that the surface becomes more stratified with surface curvature for the range of sizes simulated here.

Decreasing the size at constant temperature and surface tension is analogous to increasing temperature at constant size as the Gibbs-Thomson effect causes a depression in the melting point of the droplets at smaller sizes, $\Delta T_m \propto \gamma_{lv}/R$. However, the trends in the simulations are consistent with *decreasing* temperature. Evidently, the enhanced stratification in smaller droplets is unrelated to the size dependence of the droplet melting point.

Changes in the pressure distribution within the droplets with size show deviations from the variation observed in the planar film [Fig. 8(b)]. The compressive stresses associated with subsurface stratification of Si and Au increase and the tensile stresses within the capping monolayer in the droplets are considerably suppressed. Notably, the bulk of the droplet is strained due to the Laplace pressure that balances the surface tension. Careful examination of the size dependence of these extrema shows that their intensities increase with decreasing size, again indicating that the variation is not due to size dependence of the droplet melting point. Rather, these variations reflect the increasing strain within the bulk of the droplet that balances the surface tension. Then, the chemical excess at the surface occurs with respect to a strained bulk, and pressure effects on surface segregation become important. For a droplet so stressed, the leading order correction to the

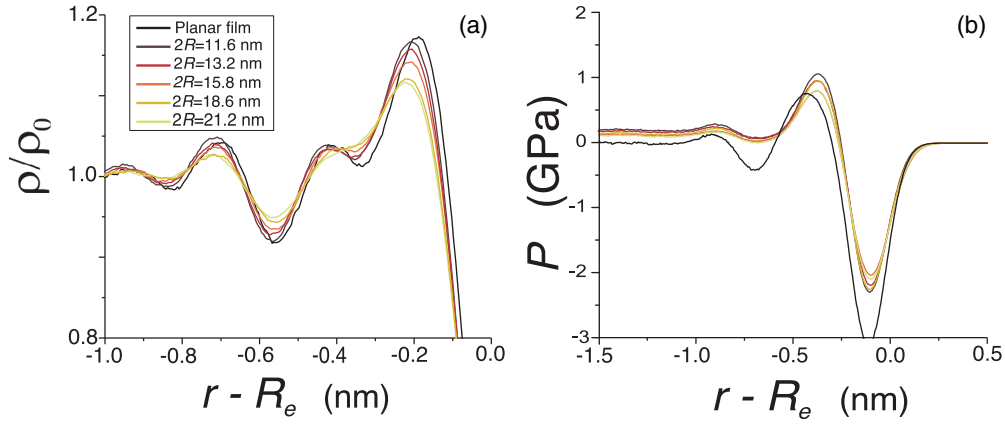

FIG. 8. Size dependence of (a) normalized radial density variation and (b) pressure distribution in equilibrated AuSi thin film and droplets with varying radii in the range $2R = 10-22$ nm, with $X_{\rm Si} = 33\%$ and at $T = 873$ K.

surface excess for each species Γ_i is [47,48]

$$\frac{\Gamma_i(p=P)}{\Gamma_i(p=0)} = \exp\left[-\frac{\langle P\rangle \Delta v_i}{RT}\right], \tag{8}$$

where Δv_i is activation volume of the segregating species at the surface and $\langle P\rangle$ is the average (external) pressure in the bulk. Equation (8) captures the effect of pressure induced atomic volume changes at the surface, with respect to the bulk, on the surface segregation. For a two component system such as the Au-Si system considered here, the activation volume is the relative change in the partial molar volumes of the two species between the surface and bulk. As an example, denoting Ω^S and Ω^B as the average partial molar volumes at the surface and bulk respectively, the change in activation volume for Au can be expressed as

$$\Delta v_{\rm Au} = \left(\Omega^S_{\rm Au} - \Omega^B_{\rm Au}\right) - \left(\Omega^S_{\rm Si} - \Omega^B_{\rm Si}\right). \tag{9}$$

Equations (8) and (9) strongly suggest that the thermodynamic interplay between the surface segregation and the pressure distribution in the droplet is mediated by the activation volume changes between the bulk and surface. They are consistent with the observed trends in the size dependence of the density and pressure distribution. For example, the increase in the Au monolayer segregation with decreasing size is a consequence of $\Delta v_{\rm Au} > 0$. Then, the combination of the tensile stress in the layer and the increasingly strained bulk of the droplet results in increase in the Au excess. Similarly, the enhanced stratification of the subsurface due to Si segregation follows from the combined effect of $\Delta v_{\rm Si} < 0$ and the fact that the Si excess is associated with a compressive stress. Then, the strained bulk of the droplet results in a decrease in Si excess in the subsurface layer with decreasing size, thereby enhancing the overall stratification of the surface layer. In the case of the planar film, the segregation is further enhanced yet the surface stress state quickly vanishes away from the bulk. As such, the activation volume changes have little effect on the surface chemical excesses.

The size dependence of the average pressure within the droplet $\langle \Delta P\rangle$ allows an independent measure of the droplet surface tension. Figure 9 shows the variation of the $\langle \Delta P\rangle$ with the droplet curvature $1/R_e$ extracted at $T = 873$ K and $X_{\rm Si} = 33\%$. The pressure differential increases almost linearly with the droplet curvature. A second-order polynomial fit based on Eq. (5) extrapolated to $R = \infty$ yields the planar surface tension, $\gamma^0_{\rm lv} = 0.582 \pm 0.01$ J/m^2. The Tolman length associated with the size effect of the surface tension is negative, $\delta = -0.5 \pm 0.1$ nm. The planar surface tension is in excellent agreement with the value extracted from computations of thin films, $\gamma^0_{\rm lv} = 0.58$ J/m^2. A negative value of the Tolman length implies a larger effective droplet radius $R_{\rm eff} = R_e - \delta > R_e$, where $R_{\rm eff}$ is the droplet radius that makes the Laplace equation exact. Its magnitude is of the order of the liquid interatomic distance, implying that the size effect is small. The surface tension associated with the effective radius, $\gamma_{\rm lv} = R_{\rm eff}/2\ \langle \Delta P\rangle$ increases nonlinearly within the narrow range $0.586-0.594$ J/m^2 with the surface curvature for droplet sizes in the range $2R = 10-30-$nm (inset, Fig. 9).

Figure 10 shows the size dependence of the density profile and the pressure distribution within the droplet below the surface crystallization temperature, $T = 600$ K and $X_{\rm Si} = 33\%$. The crystallization at the surface is confined to a single layer of thickness 0.32 nm (Fig. 6). However, we see significant

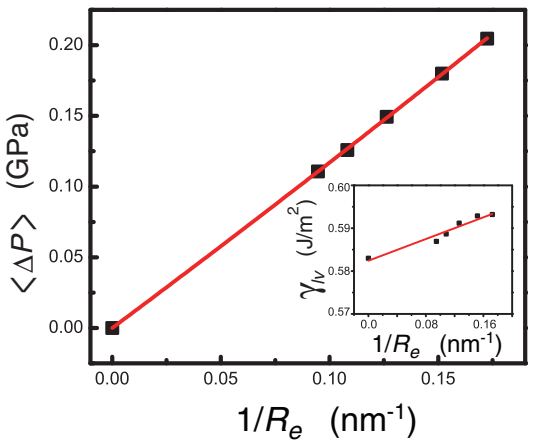

FIG. 9. Plot of the ensemble averaged pressure differential across the surface $\langle \Delta P\rangle$ vs. equimolar droplet curvature $\langle 1/R_e\rangle$ for droplets with sizes in the range $2R = 10-30$ nm. The solid red line is a second-order polynomial fit based on Eq. (5). Inset: Plot of the size dependence of the effective droplet surface tension $\gamma_{\rm lv} = R_e/2\ \langle \Delta P\rangle$.

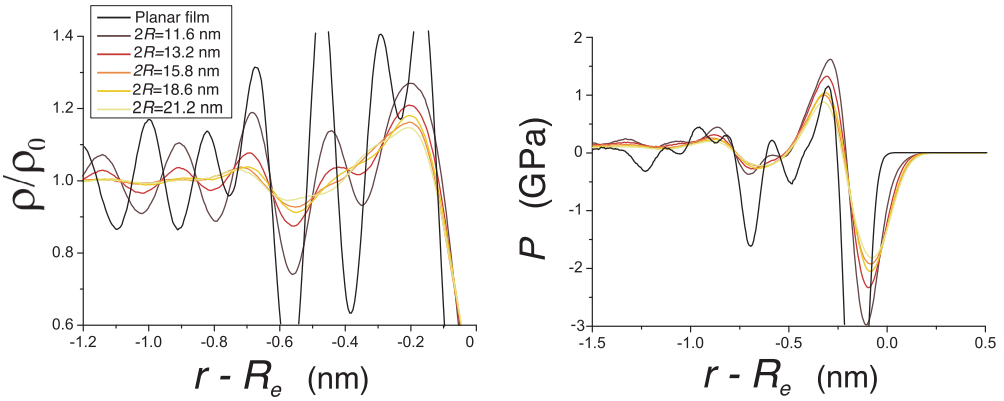

FIG. 10. Same as in Fig. 8 but for $X_{Si} = 33\%$ and at $T = 600$ K. The combination of composition and temperature is such that the surface layers of both the liquid slab and the droplets are crystallized.

changes in the density profiles compared to the planar film, also plotted for comparison. Clearly, the surface crystallization in the droplets is reduced in extent [Fig. 10(a)]. We again observe an interplay between the surface segregation and the Laplace pressure at these sizes [Fig. 10(b)], and this is evident in the density profiles for the droplet with size $2R = 21.2$ nm. While the extrema in the compression-tension at the surface associated with Au and and Si segregation are qualitatively different as the surface curvature modifies lateral order in the crystallized surface layer, for a given size the extent of the compression-tension extrema at the surface is enhanced relative to that observed above the surface crystallization temperature [Fig. 8(b)]. The layer is strained to accommodate the curvature and it results in the formation of geometrically necessary extended defects such as grain boundary scars observed in Fig. 6(c).

The Laplace pressure within the droplet leads to activation volume effects that enhance the stratification, aided by the surface curvature-induced strain in the crystalline surface phase. As the size is reduced, the crystallized layer is increasingly strained, the Laplace pressure within the droplet increases, and the linear density of the grain boundary scars on the surface increases. These three effects together set the trends in the surface segregation and pressure variation. The bulk pressure enhances the segregation due to the activation volume changes between the bulk and solidlike strained surface layer—the intensities associated with the monolayer Au and the subsurface Si increase with the increase in through-thickness stratification. The strain in the crystallized layer results in increase in the extrema of the compression-tension couple at the surface. As mentioned earlier, the increase is much more than that observed at $T = 873$ K due to the lateral order in the surface layer and this further enhances the effect of the activation volume changes between the surface and the bulk of the droplet. The grain boundary scars also serve as segregation sites for both Au and Si [Fig. 6(c)], and as their surface density increases at these small sizes, this has an added effect in amplifying the surface segregation. The combination of these effects increases overall surface segregation and stratification with decreasing size. At $2R = 11.6$ nm, the width of the stratified layer is comparable to that in the planar film, indicating that the strain in the surface layer together with the Laplace pressure effects play a dominant role in enhancing the surface crystalline order at small sizes.

The combination of these effects at $T = 600$ K also modifies the curvature dependence of the average pressure within the droplet (not shown). Unlike the behavior at $T = 873$ K, the behavior is nonlinear at high surface curvatures. The plot of the surface tension with effective radius does not show any conclusive trends at smaller sizes and exhibits large fluctuations, similar to the behavior of liquid-vapor interfaces close to a phase transition [49]. As the size decreases, we observe an increasing surface density of the grain boundary scars that separate crystallized domains on the surface layer. The nontrivial effect of these extended defects on the anisotropy in the effective surface tension additionally changes the size dependence, and we delegate these effects to a later study. Our results show that the crystallized layer fundamentally the modifies behavior of the surface layer in that its thermodynamic properties correspond to a solidlike layer that is sensitive to the surface strain as well as the size and distribution of grain boundary scars that stabilize within the surface crystal.

C. Surface phase transition

Annealing followed by controlled cooling simulations allow us to study the thermodynamics of the surface crystallization in detail. We focus on planar films and droplets with composition $X_{Si} = 33\%$. As before, the film simulations are performed on liquid slabs with in-plane periodic boundary conditions. The surface crystallization is observed over the two free surfaces using MD simulations. Each slab is relaxed for 2 ns at 800 K until the surface density profiles converge, and the average potential energy is calculated over 1-ns equilibrium simulations. In order to extract the temperature range associated with the crystallization transition and to minimize the effects of high cooling rates inherent in this approach, equilibrated configurations at 800 K are quasistatically cooled in decrements of 10 K. At each intermediate temperature, the simulation cell is again relaxed until the surface density profiles converge (within a few nanoseconds) and the average potential energy is extracted over a 1-ns equilibrium simulation thereafter.

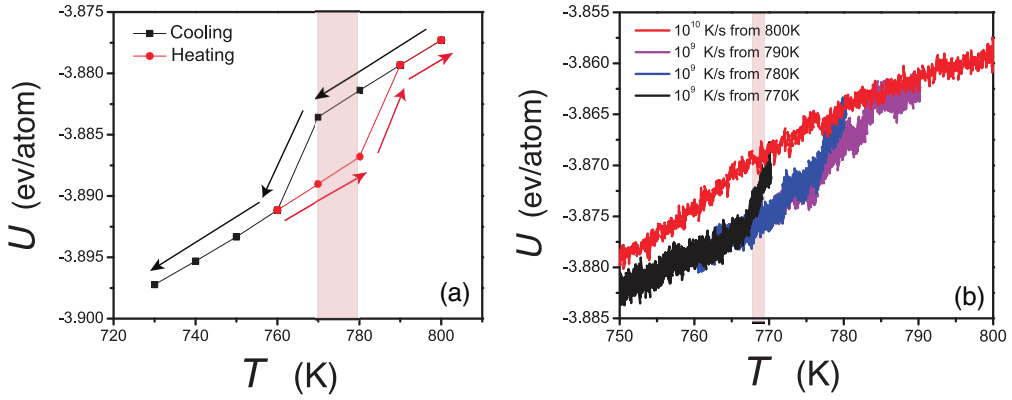

FIG. 11. (a) Potential energy per atom for a liquid AuSi ($X_{Si} = 33\%$) slab cooled and then heated quasistatically within the temperature range $T = 730-800$ K in 10 K intervals. At each intermediate temperature, the entire slab is relaxed within MD simulations for 2-ns until the segregation profile in the vicinity of each of the two free surfaces reaches a steady state. The transition temperature range $T_s^* = 760-790$ K is shown shaded in the figure. (b) Potential energy per atom for a $2R = 11.6$ nm liquid AuSi droplet with the same composition as in (a), cooled with varying initial temperatures and quench rates. The transition temperature lies in the range $T_s^* = 765-770$ K.

Figure 11(a) shows the variation in the average potential energy per atom versus temperature during the cooling cycle (black curve), averaged over the two free surfaces. The potential energy decreases with temperature, exhibits a sharp decrease from $T = 770$ K to $T = 760$ K as the surface layer crystallizes, and then recovers the much slower decrease below $T = 760$ K. The transition temperature T_s^* is strongly correlated with a slope change in $d\gamma_{lv}/dT$ [Fig. 5(b)]. The surface transition involves formation of 2D domains that rapidly grow and anneal into a single crystalline phase at $T = 760$ K. The lattice parameter of the subsurface Si within the surface crystal is identical to that observed in equilibrium surfaces, $a = 0.32$ nm. The behavior is reminiscent of a first-order transition associated with discontinuous change in the surface entropy at the transition temperature. The surface crystallization enthalpy per unit area is 0.19 J/m^2, averaged over the two surfaces.

The evolution of the average potential as the liquid slab is heated back to $T = 800$ K is also shown in Fig. 11(a) (red curve). The hysteresis in the average potential energy is negligible up to $T = 760$ K. We do not observe lateral melting of the crystallized layer beyond $T = 760$ K; rather the slab has to be superheated beyond $T = 780$ K before we recover the latent heat of formation of the surface layer. The melting is again a first-order transition that occurs in the range $T = 780-790$ K. Comparison of the heating and cooling cycles show that the transition temperatures for formation and melting of the crystalline layer are separated by at least $\Delta T = 10$ K. The asymmetry also implies that the crystallization and melting of this layer is limited by nucleation of 2D islands within the surface crystal.

The droplet MD simulations are performed at fixed size and composition, $2R = 11.6$ nm and $X_{Si} = 33\%$. Starting with an equilibrated configuration at $T = 800$ K, the droplet is continuously cooled to $T = 740$ K and then reheated. The cooling cycle results are summarized in Fig. 11(b). At high cooling rates of the order of 10^{10} K/s, the potential energy decreases continuously with a change in slope below $T = 780$ K implying that the surface crystallization is no longer a first-order transition. The cooling rates are admittedly high and can introduce artifacts. To this end, the MD simulations are performed at lower cooling rates. We observe a monotonic increase in the change of slope below $T = 780$ K. Decreasing the initial temperature within the MD simulations to closer to $T = 780$ K further increases the slope change within a narrower temperature range.

Figure 11(b) also shows the thermal evolution of the average potential energy for droplets equilibrated at $T = 790$, 780, and 770 K, and at an order of magnitude lower cooling rate of 10^9 K/s. In each case, the initial surface is laterally disordered before the droplet is quenched. For the droplet with initial temperature $T = 770$ K, lowering the temperature results in a sharp transition around $T_s^* = 767$ K that is consistent with a first-order transition, and the recovery of a slower decrease in the potential energy after the transition is complete. The potential energy change associated with the surface crystallization is 0.15 J/m^2, a small decrease over that for the planar films. This follows from the fact that the crystalline droplet surface consists of multiple ordered domains separated by grain boundary scars that remain stable as the temperature is lowered below the transition temperature. Comparison with the planar film response reveals that the transition temperature is not sensitive to the surface curvature. Reheating the droplet to above the transition temperature shows that the superheating required to melt the crystalline layer is smaller than that in the planar films (not shown), suggesting that extended defects such as grain boundary scars lower the nucleation barrier for the order-disorder transition, as expected.

IV. DISCUSSION AND CONCLUSIONS

Premelting at crystalline interfaces such as crystal surfaces and interphase/grain boundaries is a fairly common phenomenon, dating back to observations of stable thin films of water on ice below the melting point [50]. The broken symmetry at these planar defects alters the thermodynamic state of the interfacial atoms and results in enhanced disordering of the interfacial region below the bulk melting point. Thermodynamic models on the stability of the wetting liquid layer are based on the competition between bulk and interface

effects that account for the structure-based forces across the layer. The latter lead to a width dependent interface energy of the premelted layer, or a disjoining potential that sets its width [51,52]. Analogously, prefreezing at solid-liquid interfaces is a reflection of the reduction in the disorder in the abutting liquid layers as the crystalline solid imposes its structure at the interface [16,18,19,53,54].

Prefreezing on liquid surfaces tends to be system specific. It has been observed in long chain liquid polymer films, and the behavior stems from surface-mediated anisotropic chain fluctuations and interchain interactions that facilitate crystallization on the surfaces [14,55]. Surface crystallization in binary metals is driven primarily by surface segregation of the species with the lower surface tension, resulting in an almost pure crystalline surface layer that serves as a precursor for bulk crystallization [9]. In the AuSi system, Si has a lower surface tension and that drives its segregation to the surface. However, pure Si crystallization into a covalently bonded silicenelike surface layer is energetically unfavorable as it requires a stabilizing crystalline substrate. Its formation is additionally subverted by the presence of Au, evidenced by the negative enthalpy of mixing, low eutectic temperature, and glass forming properties of AuSi alloys [56]. As argued by Shpyrko *et al.* [8], this is a reflection of the structural frustration in the bulk liquid which is partially released *via* surface crystallization.

Above the surface crystallization transition temperature, our computations show that the surface layer undergoes stratification into alternating Si- and Au-rich layers. This appears to be the preferred mode for release of the structural frustration and it comes at the expense of lateral order along the surface. The spectrum of surface capillary fluctuations is consistent with the behavior of a liquid surface, that is $\langle |A(k)|^2 \rangle \propto k^{-2}$. Evidently, the lateral disorder suppresses the anisotropy in surface energetics resulting in liquidlike surface fluctuations. As the temperature is lowered below the crystallization transition temperature, the presence of the laterally ordered surface layer can lead to some deviations as the surface energy of fully crystalline interfaces typically varies with the surface orientation, and is also modified by surface stresses [57,58]. The anisotropy likely has a lesser impact for monolayer thick crystalline order on flat films, although we do not observe statistically meaningful surface fluctuations over the tens of nanosecond timescales accessible to the MD simulations, due to the combination of low temperature (and therefore diffusivities) and increased thickness of the crystallized layer.

X-ray reflectivity studies by Shpyrko *et al.* on eutectic AuSi thin films have also reported the formation of a crystalline monolayer. While its structure and stoichiometry are different ($AuSi_2$), the off-specular diffuse scattering is consistent with height-height correlations of a liquidlike surface layer [59]. It follows then that the structure of the crystalline monolayer is able to absorb changes in its inclination in accordance with the underlying stratified liquid layers, and we therefore expect to observe similar liquidlike behavior in our computations at longer timescales.

The computed values of surface tension are consistently lower than those reported in past experiments. Curve fits to the off-specular diffuse scattering data from X-ray reflectivity studies on eutectic thin films have yielded a value of $\gamma_{lv} = 0.78\ \mathrm{J/m^2}$. Naidich *et al.* have employed the large drop (LD) method to measure the temperature and composition dependence [60]. They report a value of $\gamma_{lv} = 0.86\ \mathrm{J/m^2}$ at $X_{Si} = 31\%$ and $T = 873\ \mathrm{K}$, and a slight increase to $\gamma_{lv} \approx 0.9\ \mathrm{J/m^2}$ closer to the eutectic composition $X^E_{Si} = 21\%$. Note that these LD measurements are overestimates as they were made as the droplets were cooled to ambient temperatures, yet the discrepancy with the computed values is still large and cannot be accounted by the higher eutectic composition in the model AuSi system. Surface agents such as dissolved silicon oxide and related impurities have been implicated in the Si-rich surface structure [61]. The silicon enrichment can subvert the formation of the Au capping layer, and the structural deviations can account for the increased surface tension reported in the experiments.

However, we cannot disregard limitations due to the empirical nature of the interatomic interactions used in the study. For example, the AuSi model system is based on an EAM potential for pure Au that underestimates the liquid surface tension by 20% [37]. We have addressed some of the shortcomings of this model potential in a previous study by including charge gradient corrections to the pure Au interactions [12]. The changes in the normalized density profiles are negligible. Similarly, the higher eutectic composition should not modify the trends as the Au capping layer is stable over a wide range of bulk compositions. Note that a similar disordered Au capping layer was observed in higher fidelity *ab initio* molecular dynamics studies on amorphous AuSi films [11], in accord with our computations. As such, our computations provide direct evidence that the surface crystallization is an intrinsic property of near-eutectic AuSi films.

The computations capture key qualitative trends in the temperature and composition dependence of the surface tension of AuSi thin films that are in agreement with past experiments, indicating that they are less dependent on the oxide contamination. The surface is Si-rich compared to the bulk composition over all temperature and composition ranges. The surface tension decreases with increasing X_{Si}—the trend was also observed in the LD studies and is again consistent with enhanced Si enrichment at the surface. At lower temperatures, the change in surface tension with temperature $d\gamma_{lv}/dT > 0$ and serves as direct evidence of surface crystallization in these thin films. Immediately above the transition temperature, the slope $d\gamma_{lv}/dT$ decreases as the surface becomes less stratified, yet it is still positive and the slope changes its sign at much higher temperatures when the stratification is considerably suppressed. The temperature dependence of γ_{lv} shows that segregation-induced stratification of liquid surfaces can alone lead to a positive slope $d\gamma_{lv}/dT > 0$.

The droplet studies reveal that above the surface crystallization transition, the Laplace pressure within the droplet modifies the segregation due to activation volume changes of both Au and Si between the bulk and surface, and we observe an overall increase in stratification at smaller sizes, i.e., the surface curvature modifies the activation volume differences between the bulk and the surface. Together with the fact that Si and Au segregation is associated with compressive and tensile stresses at the surface, this results in an overall increase in the through-thickness order with increasing surface curvature.

The structural changes suggest that the surface tension is size dependent. The variation of the Laplace pressure differential across the surface layer shows that the surface tension varies nonlinearly, yet the overall change is small. The Tolman length, a measure of the size dependence, is negative and of the order of the interatomic distance. This length scale is the difference between the equimolar dividing surface associated with density variations between the liquid-vapor (vacuum), and the mechanical surface through which the surface tension acts and that makes the Laplace equation exact [41]. A negative Tolman length indicates the surface tension increases as the dividing surface moves outwards, towards the vapor phase. In effect, the surface segregation increases the effective radius of the droplet, $R_e - \delta$.

The surface curvature plays a dominant role below the transition temperature. Unlike the thin films, the surface crystallized layer is strained and polycrystalline, consisting of grain boundary scars that become necessary to accommodate the large surface curvature. As a result, the order is considerably reduced compared to thin films and the effect cascades to a reduction in stratification. The compressive and tensile stresses associated with Si and Au segregation are qualitatively different due to the presence of surface strain and grain boundary scars. As the size is further reduced, we see a dramatic increase in stratification and the compression-tension couple at the surface due to an interplay between Laplace pressure driven surface segregation, surface strains that further amplify activation volume changes between the bulk and surface, and increasing density of grain boundary scars that serve as sites for segregation of Au and possibly subsurface Si. The Laplace pressure variation with size becomes increasingly nonlinear with size, indicating that the stratified layer with the surface crystalline phase no longer behaves as an effective liquid surface. Likely, the surface strain leads to surface stress based corrections to the surface energetics that render a simple capillarity based description inadequate.

Thermal cycling through the surface crystallization transition *via* nonequilibrium MD simulations reveal that for both thin films and droplets, the laterally ordered surface layer crystallizes in the range $T = 760-770$ K. The surface crystallization and melting require undercooling and superheating respectively, indicating that the phase transition is mediated by the nucleation of 2D islands. In the case of droplets, the superheating required to melt the prefrozen surface is smaller due to the presence of grain boundary scars that serve as heterogeneous sites for the melting of the crystalline layer and reduce the nucleation barrier. Although the thermal cycling rates are quite high in the MD simulations, the potential energy change at the transition temperature becomes increasingly sharp as the cooling and heating rates are reduced, confirming that the surface crystallization is a first-order phase transition. The enthalpy change is not sensitive to the thermal cycling rates, and is 0.18 and 0.15 Jm^2 for thin films and the $2R = 11.6$ nm droplet, respectively. We attribute the small decrease in the latent heat of the droplets to the presence of grain boundary scars.

The interplay between surface tension and composition of binary droplets is important for a range of applications. This is especially the case for vapor-liquid-solid growth of semiconducting nanowires. Although the size dependence of the surface tension is small for the sizes of the AuSi nanoparticles studied here, it is sensitive to temperature and composition and the latter is especially important as the nucleation and growth of nanowires grown by these routes is mediated by supersaturated droplets whose composition oscillates during growth [22,29,62].

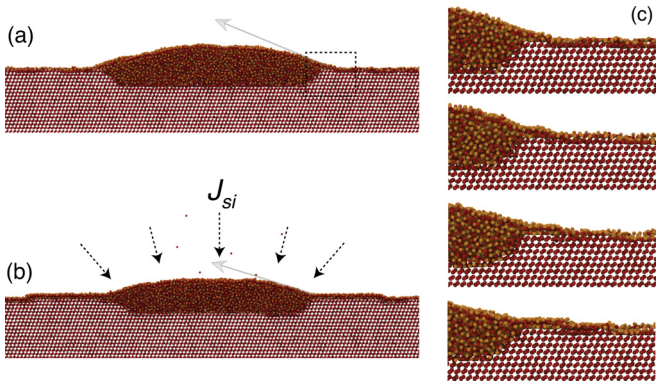

FIG. 12. (a) Atomic configuration of a quasi-2D AuSi droplet at equilibrium on a Si(111) substrate at $T = 873$ K. The equilibrium composition of the droplet is $X_{Si} = 39.5\%$. The solid-vapor layer is passivated by an Au layer. (b) Atomic configuration of the droplet-substrate system subject to constant surface current of $I_{Si} = 2$ atoms/ns at time $t = 100$ ns. Note the layer-by-layer growth at the solid-liquid interface, the reduction in the apparent contact angle, as indicated by arrows in (a) and (b), and partial growth of a new layer, referred to as a precursor wetting layer, at the solid-vapor interface. The droplet supersaturation varies between $X_{Si} = 40-42\%$. (c) Temporal evolution of the precursor wetting layer following supersaturation during the first 20 ns, showing the nucleation and growth of a precursor feet from the contact line that leads to the formation of a new layer.

To see if the effect is significant, we have performed all-atom MD simulations of the stability of an $2R = 10$ nm AuSi droplet on a Si(111) substrate. The simulations are performed above the surface crystallization temperature. The thickness of the quasi-2D droplet-substrate system is 3 nm and is sufficient to limit size effects associated with stratification of the surface layer. Figure 12(a) shows the equilibrated AuSi droplet configuration. The droplet surface is decorated by a laterally disordered Au monolayer and stratified, consistent with density profiles in isolated droplets observed in our simulations. The substrate develops {113} truncating facets as the droplet etches into the substrate until it reaches the equilibrium composition of $X_{Si} = 39.5\%$. The presence of a monolayer thick wetting layer on the solid-vapor interface composed primarily of Au atoms is critical for the stability of the droplet. As validation, we have also performed simulations with pristine Si(111) solid-vapor surfaces. The droplet rapidly becomes Si-rich and serves as a source for the Au-rich wetting layer. It quickly destabilizes the droplet, suggesting that the equilibration of the Au surface chemical potential between the liquid-vapor and solid-vapor surfaces is a crucial ingredient for the stability of the droplet. The faceted morphology of Si substrates in equilibrium with AuSi droplet and the stability of Au monolayer on the Si solid-vapor surfaces are consistent with past experiments and simulations [10,12,63].

The droplet is supersaturated by exposing it to a surface flux corresponding to a surface current of $I_{Si} = 2$ atoms/ns. The Si atoms are deposited at low kinetic energies (1 eV/atom) and directly absorbed onto the droplet surface in MD simulations. Although the surface flux is higher compared to that in experiments due to the much slower catalytic breakdown of Si precursors on AuSi surfaces [28], it is low enough such that we observe layer-by-layer growth of the Si(111) substrate, consistent with the crystallization dynamics observed during VLS growth of Si nanowires. Figure 12(b) shows the droplet-substrate system at $t = 20$ ns. The droplet is Si-rich with a silicon concentration $X_{Si} = 42\%$. Step flow is evident at the Si(111) main facet in contact with the droplet leading to layer-by-layer growth of the substrate.

The apparent contact angle of the droplet θ decreases (indicated by arrows), consistent with decrease in droplet surface tension with increasing X_{Si}. Following Young's balance along the horizontal, the contact angle is

$$\cos\theta = \frac{1}{\gamma_{lv}}(\gamma_{sv} - \gamma_{sl}\cos\alpha), \tag{10}$$

where α is the fixed angle between the (111) and (113) facets [64]. Denoting S as the spreading coefficient of the droplet, defined as

$$S = \gamma_{sv} - \gamma_{sl}\cos\alpha - \gamma_{lv} \tag{11}$$

the balance can be expressed as

$$\cos\theta = 1 + \frac{S}{\gamma_{lv}}. \tag{12}$$

At equilibrium $S < 0$ for the partial wetting droplet.

In the transient interval wherein the droplet builds up supersaturation and the Si growth is limited by nucleation, the decrease in surface tension with increasing X_{Si} requires a smaller contact angle, and also decreases the spreading coefficient S. The droplet is pinned by truncating facets and volume conservation limits the extent of change in contact angle due to deviations from a spherical cap shape. Instead, the contact line adjusts by increasing the precursor wetting layer thickness locally, i.e., γ_{sv} also decreases. The dynamics of the nucleation of this new layer from the contact line is shown in detail in Fig. 12(c). Evidently, the growth of this precursor feet is sustained by atomic surface diffusion of both Si and Au atoms from the droplet. It continues to grow to a finite distance before the Si supersaturation is absorbed by nucleation and step flow at the Si(111) solid-liquid interface. The precursor wetting layer facilitates the growth of crystallized layers that make up the base of the growing nanowire, suggesting that the eventual nanowire diameter is controlled by its extent. The growth of such microscopic layers is well known during nonequilibrium wetting of surfaces by nonvolatile droplets [65]. Our simulations highlight the role of the precursor layer, mediated by the compositional dependence of the droplet surface tension, and has ramifications for diameter selection of VLS grown nanowires.

ACKNOWLEDGMENTS

The authors are grateful for supercomputing resources available through Northeastern University and the Massachusetts Green High Performance Computing Center (MGHPCC). The study was supported by a grant from National Science Foundation DMR CMMT Program (1106214). H.W. and M.W. acknowledge support from the Fundamental Research Funds for the Central Universities, China (Grant No. WK2480000006).

[1] R. S. Wagner and W. C. Ellis, Vapor-liquid-solid mechanism of single crystal growth, Appl. Phys. Lett. **4**, 89 (1964).
[2] S. Iijima, Carbon nanotubes: Past, present and future, Physica B **323**, 1 (2002).
[3] Z. W. Pan, Z. R. Dai, and Z. L. Wang, Nanobelts of semiconducting oxides, Science **291**, 1947 (2001).
[4] T. Wada, J. Yamada, and H. Kato, Preparation of three-dimensional nanoporous si using dealloying by metallic melt and application as a lithium-ion rechargeable battery negative electrode, J. Power Sources **306**, 8 (2016).
[5] T. L. Maxwell and J. T. Balk, The fabrication and characterization of bimodal nanoporous Si with retained Mg through dealloying, Adv. Eng. Mater. **20**, 1700519 (2018).
[6] H. Reinhardt, K. Bücker, F. Yang, P. Nürnberger, and N. A. Hampp, Highly dynamic alloying and dealloying in the model system gold-silicon (AuSi), J. Phys. Chem. C **119**, 5462 (2015).
[7] O. G. Shpyrko, R. Streitel, V. S. K. Balagurusamy, A. Y. Grigoriev, M. Deutsch, B. M. Ocko, M. Meron, B. Lin, and P. S. Pershan, Surface crystallization in a liquid AuSi alloy, Science **313**, 77 (2006).
[8] O. G. Shpyrko, R. Streitel, V. S. K. Balagurusamy, A. Y. Grigoriev, M. Deutsch, B. M. Ocko, M. Meron, B. Lin, and P. S. Pershan, Crystalline surface phases of the liquid Au-Si eutectic alloy, Phys. Rev. B **76**, 245436 (2007).
[9] B. Yang, D. Gidalevitz, D. Li, Z. Huang, and S. A. Rice, Two-dimensional freezing in the liquid-vapor interface of a dilute Pb:Ga alloy, Proc. Natl. Acad. Sci. USA **96**, 13009 (1999).
[10] N. Ferralis, R. Maboudian, and C. Carraro, Temperature-induced self-pinning and nanolayering of AuSi eutectic droplets, J. Am. Chem. Soc. **130**, 2681 (2008).
[11] S.-H. Lee, J. A. Stephens, and G. S. Hwang, On the nature and origin of Si surface segregation in amorphous AuSi alloys, J. Phys. Chem. C **114**, 3037 (2010).
[12] H. Wang, L. Zepeda-Ruiz, G. H. Gilmer, and M. Upmanyu, Atomistics of vapor-liquid-solid nanowire growth, Nat. Commun. **4**, 1956 (2013).
[13] F. Panciera, J. Tersoff, A. D. Gamalski, M. C. Reuter, D. Zakharov, E. A. Stach, S. Hofmann, and F. M. Ross, Surface crystallization of liquid Au-Si and its impact on catalysis, Adv. Mater. **31**, 1806544 (2019).
[14] S. Prasad, Z. Jiang, S. K. Sinha, and A. Dhinojwala, Partial Crystallinity in Alkyl Side Chain Polymers Dictates Surface Freezing, Phys. Rev. Lett. **101**, 065505 (2008).
[15] Y. Yang, M. Asta, and B. B. Laird, Solid-Liquid Interfacial Premelting, Phys. Rev. Lett. **110**, 096102 (2013).
[16] A.-K. Löhmann, T. Henze, and T. Thurn-Albrecht, Direct observation of prefreezing at the interface melt–solid in poly-

mer crystallization, Proc. Natl. Acad. Sci. USA **111**, 17368 (2014).
[17] Y. Yang, D. L. Olmsted, M. Asta, and B. B. Laird, Atomistic characterization of the chemically heterogeneous Al-Pb solid-liquid interface, Acta Mater. **60**, 4960 (2012).
[18] J. P. Palafox-Hernandez, B. B. Laird, and M. Asta, Atomistic characterization of the Cu-Pb solid-liquid interface, Acta Mater. **59**, 3137 (2011).
[19] B. B. Laird and R. L. Davidchack, Wall-induced prefreezing in hard spheres: A thermodynamic perspective, J. Phys. Chem. C **111**, 15952 (2007).
[20] S. M. Roper, S. H. Davis, S. A. Norris, A. A. Golovin, P. W. Voorhees, and M. Weiss, Steady growth of nanowires via the vapor-liquid-solid method, J. Appl. Phys. **102**, 034304 (2007).
[21] S. N. Mohammad, Analysis of the vapor-liquid-solid mechanism for nanowire growth and a model for this mechanism, Nano Lett. **8**, 1532 (2008).
[22] K. W. Schwarz and J. Tersoff, From Droplets to Nanowires: Dynamics of Vapor-Liquid-Solid Growth, Phys. Rev. Lett. **102**, 206101 (2009).
[23] E. I. Givargizov and A. A. Chernov, Growth rate of crystal whiskers grown by the vapor-liquid-crystal mechanism, and role of surface energy, Kristallografiya **18**, 147 (1973).
[24] E. I. Givargizov, Fundamental aspects of VLS growth, J. Crys. Growth **31**, 20 (1975).
[25] S. Kodambaka, J. Tersoff, M. C. Reuter, and F. M. Ross, Diameter-Independent Kinetics in the Vapor-Liquid-Solid Growth of Si Nanowires, Phys. Rev. Lett. **96**, 096105 (2006).
[26] B. J. Kim, J. Tersoff, S. Kodambaka, M. C. Reuter, E. A. Stach, and F. M. Ross, Kinetics of individual nucleation events observed in nanoscale vapor-liquid-solid growth, Science **322**, 1070 (2008).
[27] T. David, D. Buttard, T. Schülli, F. Dallhuin, and P. Gentile, Structural investigation of silicon nanowires using GIXD and GISAXS: Evidence of complex saw-tooth faceting, Surf. Sci. **602**, 2675 (2008).
[28] B. J. Kim, J. Tersoff, C. Y. Wen, M. C. Reuter, E. A. Stach, and F. M. Ross, Determination of Size Effects During the Phase Transition of a Nanoscale Au-Si Eutectic, Phys. Rev. Lett. **103**, 155701 (2009).
[29] C.-Y. Wen, J. Tersoff, K. Hillerich, M. C. Reuter, J. H. Park, S. Kodambaka, E. A. Stach, and F. M. Ross, Periodically Changing Morphology of the Growth Interface in Si, Ge, and GaP Nanowires, Phys. Rev. Lett. **107**, 025503 (2011).
[30] E. R. Hemesath, D. K. Schreiber, E. B. Gulsoy, C. F. Kisielowski, A. K. Petford-Long, P. W. Voorhees, and L. J. Lauhon, Catalyst incorporation at defects during nanowire growth, Nano Lett. **12**, 167 (2012).
[31] A. M. Dongare, M. Neurock, and L. V. Zhigilei, A new angular-dependent embedded-atom-method potential for atomistic simulations of metal-covalent systems, Phys. Rev. B **80**, 184106 (2009).
[32] S. M. Foiles, Calculation of the surface segregation of Ni-Cu alloys with the use of the embedded-atom method, Phys. Rev. B **32**, 7685 (1985).
[33] M. P. Allen and D. J. Tildesley, *Computer Simulation of Liquids* (Oxford University Press, Oxford, 1989).
[34] F. P. Buff, R. A. Lovett, and F. H. Stillinger, Interfacial Density Profile for Fluids in the Critical Region, Phys. Rev. Lett. **15**, 621 (1965).
[35] J. D. Weeks, Structure and thermodynamics of the liquid-vapor interface, J. Chem. Phys. **67**, 3106 (1977).
[36] W. Yu and D. Stroud, Molecular dynamics study of surface segregation in liquid semiconductor alloys, Phys. Rev. B **56**, 12243 (1997).
[37] E. B. Webb III and G. S. Grest, Liquid/Vapor Surface Tension of Metals: Embedded Atom Method with Charge Gradient Corrections, Phys. Rev. Lett. **86**, 2066 (2001).
[38] V. Vitek and T. Egami, Atomic level stresses in solids and liquids, Phys. Status Solidi B **144**, 145 (1987).
[39] A. Karma, Fluctuations in solidification, Phys. Rev. E **48**, 3441 (1993).
[40] J. S. Rowlinson and B. Widom, *Molecular Theory of Capillarity* (Clarendon Press, Oxford, 1982).
[41] R. C. Tolman, Consideration of the Gibbs theory of surface tension, J. Chem. Phys. **16**, 758 (1948).
[42] R. C. Tolman, The effect of droplet size on surface tension, J. Chem. Phys. **17**, 333 (1949).
[43] H. W. Zhang, T. Balasubramanian, and R. I. G. Uhrberg, Core level photoelectron spectroscopy study of the Au/Si(111) 5×2, $\alpha - \sqrt{3} \times \sqrt{3}$, $\beta - \sqrt{3} \times \sqrt{3}$, and 6×6 surfaces, Phys. Rev. B **65**, 035314 (2001).
[44] S. Mechler, P. S. Pershan, E. Yahel, S. E. Stoltz, B. Lin, O. G. Shpyrko, M. Meron, and S. Sellner, Self-Consistent Interpretation of the 2D Structure of the Liquid $Au_{82}Si_{18}$ Surface: Bending Rigidity and the Debye-Waller Effect, Phys. Rev. Lett. **105**, 186101 (2010).
[45] A. R. Bausch, M. J. Bowick, A. Cacciuto, A. D. Dinsmore, M. F. Hsu, D. R. Nelson, M. G. Nikolaides, A. Travesset, and D. A. Weitz, Grain boundary scars and spherical crystallography, Science **299**, 1716 (2003).
[46] L. Peng, E. Ringe, R. P. Van Duyne, and L. D. Marks, Segregation in bimetallic nanoparticles, Phys. Chem. Chem. Phys. **17**, 27940 (2015).
[47] D. McLean, *Grain Boundaries in Metals* (Oxford University Press, Oxford, 1957).
[48] P. Lejcek, *Grain Boundary Segregation in Metals* (Springer-Verlag, Berlin, 2010).
[49] A. E. van Giessen and E. M. Blokhuis, Direct determination of the Tolman length from the bulk pressures of liquid drops via molecular dynamics simulations, J. Chem. Phys. **131**, 164705 (2009).
[50] U. Dahmen, S. Hagege, F. Faudot, T. Radetic, and E. Johnson, Observations of interface premelting at grain-boundary precipitates of Pb in Al, Philos. Mag. B **84**, 2651 (2004).
[51] S. J. Fensin, D. Olmsted, D. Buta, M. Asta, A. Karma, and J. J. Hoyt, Structural disjoining potential for grain-boundary premelting and grain coalescence from molecular-dynamics simulations, Phys. Rev. E **81**, 031601 (2010).
[52] J. J. Hoyt, Z. T. Trautt, and M. Upmanyu, Fluctuations in molecular dynamics simulations, Math. Comput. Simul. **80**, 1382 (2010).
[53] H. Reichert, O. Klein, H. Dosch, M. Denk, V. Honkimäki, T. Lippmann, and G. Reiter, Observation of five-fold local symmetry in liquid lead, Nature **408**, 839 (2000).
[54] M. Dijkstra, Capillary Freezing or Complete Wetting of Hard Spheres in a Planar Hard Slit? Phys. Rev. Lett. **93**, 108303 (2004).
[55] X. Z. Wu, B. M. Ocko, E. B. Sirota, S. K. Sinha, M. Deutsch, B. H. Cao, and M. W. Kim, Surface tension measurements of

surface freezing in liquid normal alkanes, Science **261**, 1018 (1993).

[56] W. Klement, R. H. Willens, and P. Duwez, Non-crystalline structure in solidified gold-silicon alloys, Nature **187**, 869 (1960).

[57] D. Sander, Surface stress: Implications and measurements, Curr. Opin. Solid State Mater. Sci. **7**, 51 (2003).

[58] M. Schmid, W. Hofer, P. Varga, P. Stoltze, K. W. Jacobsen, and J. K. Norskov, Surface stress, surface elasticity and the size effect in surface segregation, Phys. Rev. B **51**, 10937 (1995).

[59] A. Braslau, P. S. Pershan, G. Swislow, B. M. Ocko, and J. Als-Nielsen, Capillary waves on the surface of simple liquids measured by X-ray reflectivity, Phys. Rev. A **38**, 2457 (1988).

[60] Y. V. Naidich, V. M. Perevertailo, and L. P. Obushchak, Density and surface tension of alloys of the systems Au-Si and Au-Ge, Sov. Powder Metall. Met. Ceram **14**, 403 (1975).

[61] V. Halka, R. Streitel, and W. Freyland, Is surface crystallization in liquid eutectic AuSi surface-induced? J. Phys.: Cond. Matt. **20**, 355007 (2008).

[62] S. H. Ho, M. F. Chisholm, Y. Kauffmann, W. D. Kaplan, W. Luo, M. Rühle, and C. Scheu, Oscillatory mass transport in vapor-liquid-solid growth of sapphire nanowires, Science **330**, 489 (2010).

[63] J. B. Hannon, S. Kodambaka, F. M. Ross, and R. M. Tromp, The influence of the surface migration of gold on the growth of silicon nanowires, Nature **440**, 69 (2006).

[64] We have ignored torque terms associated with solid-liquid and solid-vapor interfaces in the balance under the assumption that the cusps in the γ-plot are sufficiently deep.

[65] M. N. Popescu, G. Oshanin, S. Dietrich, and A.-M. Cazabat, Precursor films in wetting phenomena, J. Phys.: Condens. Matter **24**, 243102 (2012).